# Detection of single nano-defects in photonic crystals between crossed polarizers

**Jon Olav Grepstad,**[1,*] **Peter Kaspar,**[2] **Ib-Rune Johansen,**[3] **Olav Solgaard,**[4] **and Aasmund Sudbø**[5,6]

[1]*Department of Electronics and Telecommunications, Norwegian University of Science and Technology, NO-7491 Trondheim, Norway*
[2]*III-V Lab, a joint lab of Alcatel-Lucent Bell Labs, Thales Research & Technology, and CEA Leti, F-91767 Palaiseau, France*
[3]*SINTEF ICT, Microsystems and Nanotechnology, NO-0373, Norway*
[4]*E.L. Ginzton Laboratory, Stanford University, CA-94305, USA*
[5]*Department of Physics, University of Oslo, NO-0316, Norway*
[6]*University Graduate Center, NO-2027 Kjeller, Norway*

[*]*jonolav.grepstad@sintef.no*

**Abstract:** We investigate, by simulations and experiments, the light scattering of small particles trapped in photonic crystal membranes supporting guided resonance modes. Our results show that, due to amplified Rayleigh small particle scattering, such membranes can be utilized to make a sensor that can detect single nano-particles. We have designed a biomolecule sensor that uses cross-polarized excitation and detection for increased sensitivity. Estimated using Rayleigh scattering theory and simulation results, the current fabricated sensor has a detection limit of 26 nm, corresponding to the size of a single virus. The sensor can potentially be made both cheap and compact, to facilitate use at point-of-care.

## References and links

1. B. Bohunicky and S. A. Mousa, "Biosensors: the new wave in cancer diagnosis," Nanotechnol. Sci. Appl. **4**, 1–10 (2010).
2. M. U. Ahmed, I. Saaem, P. C. Wu, and A. S. Brown, "Personalized diagnostics and biosensors: a review of the biology and technology needed for personalized medicine," Crit. Rev. Biotechnol. (2013).
3. M. F. Pineda, L. L. Chan, T. Kuhlenschmidt, C. J. Choi, M. Kuhlenschmidt, and B. T. Cunningham, "Rapid specific and label-free detection of porcine rotavirus using photonic crystal biosensors," IEEE Sens. J. **9**, 470–477 (2009).
4. D. Duval and L. M. Lechuga, "Breakthroughs in photonics 2012: 2012 breakthroughs in lab-on-a-chip and optical biosensors," IEEE Photonics J. **5**, 0700906 (2013).
5. F. Vollmer and L. Yang, "Label-free detection with high-q microcavities: a review of biosensing mechanisms for integrated devices," Nanophotonics **37**, 267–291 (2012).
6. R. Bruck, E. Melnik, P. Muellner, R. Hainberger, and M. Lammerhofer, "Integrated polymer-based mach-zehnder interferometer label-free streptavidin biosensor compatible with injection molding," Biosens. Bioelectron. **26**, 3832–3837 (2011).
7. D. Duval, J. Osmond, S. Dante, C. Dominguez, and L. Lechuga, "Grating couplers integrated on mach-zehnder interferometric biosensors operating in the visible range," IEEE Photonics J. **5**, 3700108 (2013).
8. M. Mancuso, J. M. Goddard, and D. Erickson, "Nanoporous polymer ring resonators for biosensing," Opt. Express **20**, 245–255 (2012).

9. V. R. Dantham, S. Holler, C. Barbre, D. Keng, V. Kolchenko, and S. Arnold, "Label-free detection of single protein using a nanoplasmonic-photonic hybrid microcavity," Nano Lett. **13**, 3347–3351 (2013).
10. S. Pal, P. M. Fauchet, and B. L. Miller, "1-d and 2-d photonic crystals as optical methods for amplifying biomolecular recognition," Anal. Chem. **84**, 8900–8908 (2012).
11. I. Ament, J. Prasad, A. Henkel, S. Schmachtel, and C. Sonnichsen, "Single unlabeled protein detection on individual plasmonic nanoparticles," Nano Lett. **12**, 1092–1095 (2012).
12. P. Zijlstra, P. M. R. Paulo, and M. Orrit, "Optical detection of single non-absorbing molecules using the surface plasmon resonance of a gold nanorod," Nat. Nanotechnol. **7**, 379-382 (2012).
13. R. Adato and H. Altug, "In-situ ultra-sensitive infrared absorption spectroscopy of biomolecule interactions in real time with plasmonic nanoantennas," Nat. Commun. **4**, 2154 (2013).
14. A. E. Cetin and H. Altug, "Fano resonant ring/disk plasmonic nanocavities on conducting substrates for advanced biosensing," ACS Nano **6**, 9989–9995 (2012).
15. A. A. Yanik, M. Huang, O. Kamohara, A. Artar, T. W. Geisbert, J. H. Connor, and H. Altug, "An optofluidic nanoplasmonic biosensor for direct detection of live viruses from biological media," Nano Lett. **10**, 4962–4969 (2010).
16. M. E. Beheiry, V. Liu, S. Fan, and O. Levi, "Sensitivity enhancement in photonic crystal slab biosensors," Opt. Express **18**, 22702–22714 (2010).
17. J. O. Grepstad, P. Kaspar, O. Solgaard, I.-R. Johansen, and A. S. Sudbø, "Photonic-crystal membranes for optical detection of single nano-particles, designed for biosensor application," Opt. Express **20**, 7954–7965 (2012).
18. C. Ge, M. Lu, S. George, T. A. Flood, C. Wagner, J. Zheng, A. Pokhriyal, J. G. Eden, P. J. Hergenrother, and B. T. Cunningham, "External cavity laser biosensor," Lab Chip **13**, 1247–1256 (2013).
19. S. Fan and J. D. Joannopoulos, "Analysis of guided resonances in photonic crystal slabs," Phys. Rev. B **65**, 235112 (2002).
20. V. Lousse, W. Suh, O. Kilic, S. Kim, O. Solgaard, and S. Fan, "Angular and polarization properties of a photonic crystal slab mirror," Opt. Express **12**, 1575–1582 (2004).
21. W. Suh, M. F. Yanik, O. Solgaard, and S. Fan, "Displacement-sensitive photonic crystal structures based on guided resonance in photonic crystal slabs," Appl. Phys. Lett. **82**, 1999–2001 (2003).
22. O. Kilic, S. Kim, W. Suh, Y.-A. Peter, A. S. Sudbø, M. F. Yanik, S. Fan, and O. Solgaard, "Photonic crystal slabs demonstrating strong broadband suppression of transmission in the presence of disorders," Opt. Lett. **29**, 2782–2784 (2004).
23. M. Huang, A. A. Yanik, T. Y. Chang, and H. Altug, "Sub-wavelength nanofluidics in photonic crystal sensors," Opt. Express **17**, 24224–24233 (2009).
24. J. O. Grepstad, P. Kaspar, O. Solgaard, I.-R. Johansen, and A. Sudbo, "Optical imaging system designed for biosensing using a photonic crystal membrane to detect nanoparticles," in *Imaging and Applied Optics Technical Papers* (Optical Society of America, 2012), pp. IM4C.2.
25. J. Voros, "The density and refractive index of adsorbing protein layers," Biophys. J. **87**, 553–561 (2004).
26. Commercially available software, OptiFDTD 9.0, supplied by Optiwave, http://optiwave.com/, visited 25 Oct. 2013.
27. Commercially available software supplied by KJ Innovation, http://software.kjinnovation.com/GD-Calc.html, visited 25 Oct. 2013.
28. J.-P. Berenger, "Numerical reflection from FDTD-PMLs: a comparison of the split PML with the unsplit and CFS PMLs," IEEE Trans. Antennas Propag. **50**, 258–265 (2002).
29. J. O. Grepstad, M. Greve, B. Holst, I.-R. Johansen, O. Solgaard, and A. Sudbo, "Finite-size limitations on quality factor of guided resonance modes in 2d photonic crystals," Opt. Express **21**, 23640–23654 (2013).
30. C. F. Bohren and D. R. Huffman, *Absorbtion and Scattering of Light by Small Particles* (John Wiley, 1998), Chap. 5.
31. J. O. Grepstad, M. Greve, T. Reisinger, and B. Holst, "Nano-structuring on free-standing, dielectric membranes using e-beam lithography," J. Vac. Sci. Technol. B **31**, 06F402 (2013).

---

# 1. Introduction

Preventive action and early detection of diseases are identified among the best and most cost efficient means of improving health care [1, 2]. This can be done by developing efficient high sensitivity biosensors that are cheap and small, allowing them to be applied by physicians at point-of-care or even as a personal appliance in the comfort of our own homes. A technology proposed to realize these next generation biosensors, is label-free optical biosensing [3, 4]. Label-free optical sensors can be made using micro- and nano-technology that generally provides devices that are cheap and small. These sensors also have some of the highest sensitivities reported today [5].

All label-free optical biosensors are based on the same two basic principles. Firstly, a surface is furnished with molecules that can capture a specific targeted molecule. The capture process is generally a time-efficient one-step reaction, in contrast to label or tag assisted detection, where a radioactive or fluorescent molecule is added to captured target molecules through a multilevel chemical reaction. Secondly, the surface is optically designed to enable concentration of light, from an excitation source, at the specific areas where captured molecules are made to settle. This induces an optical response that is sensitive to changes in permittivity in the capture zone. Capture events typically manifest themselves as a shift in resonance frequency, a dip in transmission or reflection, or as scattering. Label-free biosensors can hence be considered to be composed of two parts: A chemistry that provides selectivity and an optical transducer that provides sensitivity. The focus of this article will be the optical transducer.

A number of different transducers exist. Mach-Zehnder interferometers [6, 7], optical ring resonators [8, 9], photonic crystal cavity resonators [10], and techniques exploiting local surface-plasmon-resonance (LSPR) in metal nano-particles are promising. Some are even reported to sense changes in refractive index corresponding to a single molecule [5, 9, 11, 12]. Some of the above transducers do however call for elaborate alignment procedures in order to couple light in and out of the transducer, and they all require complex designs to achieve a high dynamic range. Consequently, these schemes seem more applicable as laboratory tools, and less suitable in cheap and compact point-of-care devices. Sensors exploiting surface-plasmon-resonance in periodic metal nano-structures [13–15], and photonic crystal sensors exploiting coupling to guided resonance modes [16–18], have so far not reached single-molecule sensitivity. These do in general have lower sensitivities, but are advantageous regarding in- and out coupling of light and can be made with a high dynamic range.

In a recent report [17], we presented a photonic crystal based biosensor that exploits coupling to guided resonance modes [19]. The transducer is composed of a membrane, where a periodic square lattice of holes has been etched through the membrane. This creates a periodic permittivity in the membrane plane that allows normal incident light to couple into in-plane propagating modes. The particular mode that we excite, concentrates its field in the vicinity of the membrane, primarily in the holes. It also produces a sharp dip in the reflected spectrum.

The center wavelength of the dip in reflectivity is highly sensitive to changes in permittivity close to the membrane, especially at the hole walls, where the field is maximized. Covering a pristine 2D PC membrane with a monolayer of biomolecules that has different permittivity than the surrounding media, will hence shift the center wavelength of the dip, allowing the monolayer to be detected. However, when aiming for sensitivities on the order of single molecules, captured molecules cannot be considered to be a monolayer. Single capture events are locally bound defects that break the symmetry of the lattice. The defects will induce local shifts in the frequency of resonant modes, but they will also provide new exit channels for light semi-bound in the guided resonance mode. It is the latter effect that we exploit in our sensor. The membrane is designed for high reflectivity in its native state [20–22], at a chosen operating wavelength. When a particle is trapped in a hole, it will be located in a strong optical field that is scattered out of the membrane. Consequently, a bright spot on a dark background, centered at the origin of the particle, can be detected in transmission. Furthermore, the choice of making an intensity based sensor, using a single operating wavelength, instead of tracking a shift in the resonance, limits the required number of optical components in the design. This is advantageous in relation to cost and compactness of a final device.

In [17], we proposed that the detection principle can be modeled as enhanced Rayleigh scattering. The current report is an extension of this work. We now present simulation and experimental results that support our hypothesis. A modified optical setup is also presented, where crossed polarizers [23] are used to suppresses the background and increases the signal-to-noise

ratio. Using the new optical setup, we calculate a detection limit corresponding to single particles the size of viruses.

## 2. Images obtained with unpolarized light

Figure 1(a) shows a scanning electron microscope (SEM) image of the front side of a fabricated 2D photonic crystal (PC) membrane. It is composed of a square lattice of $100 \times 100$ holes with radius $145 \pm 10$ nm and period $490 \pm 5$ nm. The holes are etched through three thin films, $50 \pm 5$ nm $Si_3N_4$/$50 \pm 5$ nm $SiO_2$/$50 \pm 5$ nm $Si_3N_4$, free-standing in air. This is the transducer in our sensor. The motivation for choosing a three layered stack, is that a cylinder surface is then define inside every hole, chemically different from the rest of the PC surface. In turn, this can enable us to functionalize the inside of the holes to capture targeted molecules, while the rest of the PC opposes molecule capture. A more detailed description of how molecules can be immobilized in our structure is given in previous work [17].

Figure 1(b) shows a SEM image of the membrane backside, and Fig. 1(c) is an image of the front side of the membrane recorded with an optical microscope. Two defects or contaminations are visible in all the images, SEM as well as optical. The discrepancy located at the top in Fig. 1(a), resulting in the upper bright spot in Fig. 1(c), is not visible in Fig. 1(b). It hence lies on the front side, and is known to be a contamination. It first appeared on the surface sometime after fabrication. The left defect is especially well suited for preliminary studies. It is located inside a hole, where we plan to capture biomolecules, and has a radius of $60 \pm 15$ nm. We will refer to it as defect A. The permittivity of the defect is unknown, but can be limited by possible contaminations in our lab, that have a permittivity between 2 and 12.25.

From Fig. 1(b), showing the backside of the PC, it appears like defect A results from a hole that has not been fully etched. This suggests that defect A is composed of a mix of $Si_3N_4$ and $SiO_2$, and has a permittivity between 2.25 and 4 for visible light. The lower limit is comparable to the permittivity of relevant biological target molecules, which typically have a permittivity between 2 and 2.5 [25].

The setup used for optical characterization, is shown in Fig. 1(d). It is composed of a narrowband light source irradiating the backside of the fabricated PC, and a microscope connected to a CCD camera recording the transmitted light with spatial resolution. Two polarizers are placed in the light path, one between the source and the PC, and a second between the PC and the CCD camera. We return to results generated with polarizers $L_s$ and $L_d$ employed, and a laser diode source in section 4. For now, we will focus on the image in Fig. 1(c), recorded with a light source in the form of a halogen lamp routed through a monochromator, and without the polarizers $L_s$ and $L_d$ in the light path [24]. The image depicts the unpolarized transmittance of the membrane, for narrowband unpolarized light, normally incident on the backside of the membrane at a center wavelength of 632 nm.

We have previously [17] proposed that the appearance of a particle trapped in a PC, as shown by the bright spot pattern in Fig. 1(c), can be understood as amplified Rayleigh small particle scattering. Provided that a particle trapped in a PC is sufficiently small, the mode field will not be affected by its presence. This results in the overall transmittance being low, and the field in the vicinity of the membrane being high. The mode field hence acts as a driving field, causing particles that are trapped in the lattice to scatter the resonantly enhanced field in the membrane. Scattered light will exit out into the surrounding medium as spherical waves with origin at the particle center, and can be refocused to form bright spots on a detector.

A closer examination of the bright spot pattern in Fig. 1(c), reveals that this description of the situation is inadequate. The pattern is composed of an ensemble of spots that follow the symmetry of the lattice.

a    SEM image – Front side of PC

b    SEM image - Backside of PC

c    Optical microscope image
     Unpolarized source and detection

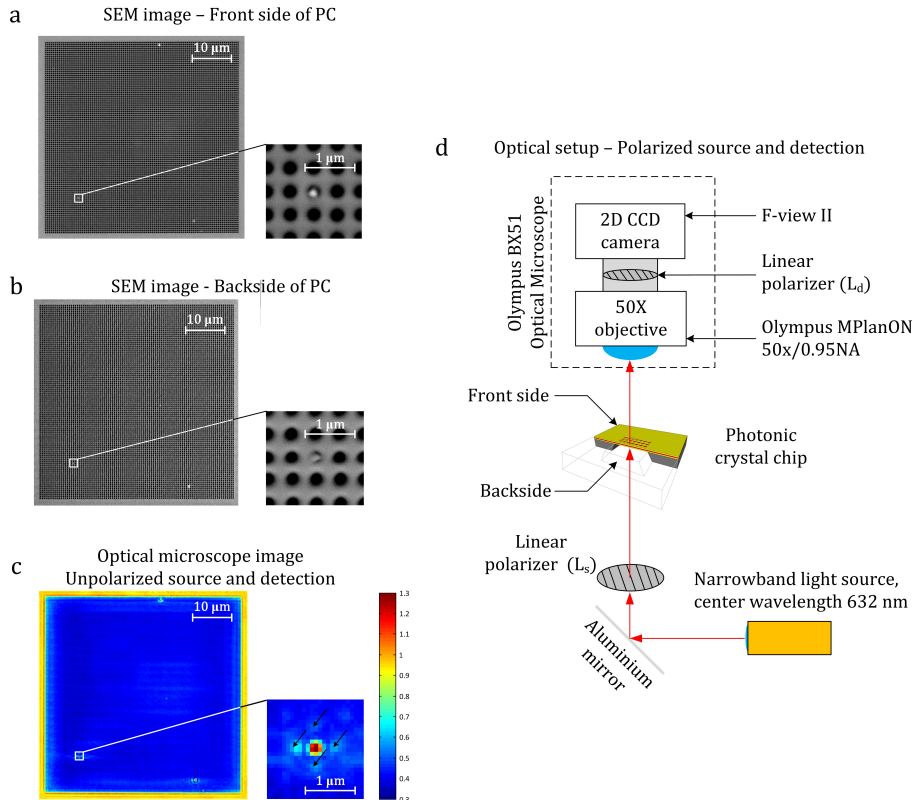d    Optical setup – Polarized source and detection

Fig. 1. Images acquired using a scanning electron microscope (SEM) of the front side (a) and backside (b) of a fabricated sample of the photonic crystal. An area of the image showing a particle with a radius of $60\pm15$ nm has been enlarged. The particle is a defect in the lattice. (c) An image of the crystal, front side facing up, has been recorded using an optical setup [24] with monochromatic illumination at 632 nm, normally incident from the backside. The color scale gives the transmittance of the membrane. (d) Optical setup with a collimated narrowband light source centered at 632 nm, emitting a beam directed by a 45° aluminum mirror to the backside of a photonic crystal at normal incidence, via a linear polarizer, $L_s$. Transmitted light is collected by a 50x/0.95 NA objective lens, passes through a linear polarizer, $L_d$, and is recorded by a 2D CCD camera. The image displayed in (c) is recorded with the optical setup in (d), not using polarizers $L_s$ and $L_d$.

## 3. Simulation of particles trapped in 2D photonic crystals

Finite-difference-time-domain (FDTD) simulations [26] and rigorously coupled wave analysis (RCWA) [27], have been done to further investigate the effect of placing a small particle in a 2D PC.

Results from simulation using RCWA are summarized in Fig. 2. A unit cell in the fabricated PC, with nominal dimensions, is illustrated in Fig. 2(a). Figure 2(b) shows the simulated transmittance of the perfectly periodic PC as a function of wavelength, for normal incidence light. Two dips in transmission can be seen in the plot, resulting from coupling of incident light to two guided-resonance modes. We utilize the mode causing the low-transmission dip at 631 nm. The simulated spectrum in Fig. 2(b) agrees well with the transmitted spectrum of the fabricated structure, as we have shown earlier [17], but is slightly shifted with respect to the measured
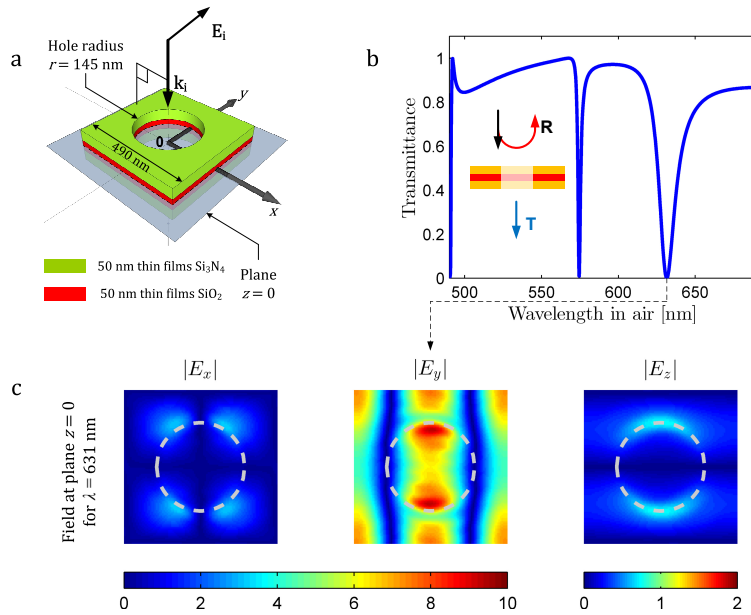
Fig. 2. Results from RCWA simulations. (a) Unit cell of a 2D photonic crystal membrane, and (b) the simulated transmittance of the crystal for normal incidence $y$-polarized light as a function of wavelength. (c) Color image representations of the resonantly enhanced field at the center plane, $z = 0$, is given for the dip at 631 nm. The bottom color scale gives the field amplitude, relative to the amplitude of the incident field.

dip value at 632 nm. A simulation showing the field in the center plane of a unit cell of the membrane at this wavelength, for incident light polarized in the $y$-direction, is given in Fig. 2(c). The $y$ component of the mode field forms a saddle profile aligned with the $y$-axis, peaking at the hole walls with an amplitude 10 times the incident amplitude. Inside the holes, the $x$ and $z$ component are an order of magnitude or more smaller than the $y$ component. Note that it is the absolute value of the field that is plotted in Fig. 2. Crossing zero field nodes, the phase of the fields change by a factor $\pi$.

The design of the FDTD simulation is illustrated in Fig. 3. A volume, having a refractive index of air, $n_0 = 1$, with a length corresponding to four lattice periods, $4p$, and a cross section of $15p \times 15p$, was defined. The spatial resolution was set to 20 nm in the $z$-direction, and 10 nm in the $x$- and $y$-direction. A slab with refractive index $n_s = 2$ was centered at $z = p$. The thickness of the slab was set to 160 nm and the unit cell in the lattice is composed of a hole going through the slab with a radius of $r = 145$ nm. The lattice is square with a period $p = 500$ nm. All simulation boundaries are terminated with absorbing layers of the perfectly matched type (PML) [28].

First, the frequency response of the PC was analyzed. This was done by imposing a planar Gaussian pulse, truncated at the simulation boundaries, with normal incidence relative to the membrane plane at $z = 0.5p$, with center frequency corresponding to a vacuum wavelength of 650 nm. The frequency response was found by calculating the Fourier transform of the amplitude of the transmitted wave, recorded at $z = 4p$ in the center of the simulation domain on the $xy$-plane. This allowed us to find the wavelength where the simulated PC supports the particular mode field corresponding to the one displayed in Fig. 2(c). The simulated design is not identical to the fabricated PCs, but has been modified to speed up the simulations. The
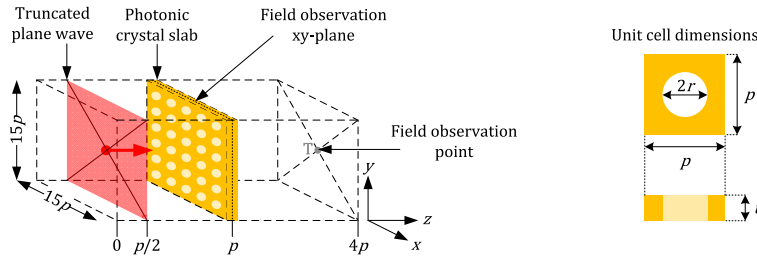
Fig. 3. (Left) Illustration of the FDTD simulation domain, composed of a volume of air, with refractive index set to $n_{air} = 1$, measuring $15 \times 15 \times 4$ periods, where the period $p = 500$ nm. All simulation boundaries are terminated with absorbing layers of the perfectly matched type (PML). A plane incident wave, truncated at the simulation boundaries, is imposed at $z = 0.5p$, traveling in the positive $z$-direction, and a photonic crystal membrane with thickness $t = 160$ nm is centered at $z = p$, aligned with the $xy$-plane. The field is recorded as a function of time at the observation point T, and the terminal field distribution is recorded at the $xy$-plane at $z = p$. (Right) Drawing of the unit cell in the photonic crystal. The period is $p$, and the radius of the hole is $r = 145$ nm. The membrane material has a refractive index set to $n_{memb} = 2$, corresponding to $Si_3N_4$.

transmission spectra of the simulated and fabricated PC are therefore shifted relative to each other, due to the small differences in materials, lattice period and membrane thickness. The dip in transmission at 703.6 nm for the simulated PC, and the dip at 632 nm for the fabricated PC, are both caused by the same guided resonance mode.

Simulations using a continuous wave source tuned to 703.6 nm were thereafter performed for a pristine PC and for a PC with one particle, vertically centered, in the center hole. This was done by imposing a plane wave, truncated at the simulation boundaries, with normal incidence relative to the membrane plane at $z = 0.5p$, traveling in the positive $z$-direction. The fields in the center plane of the PC were observed. Three lateral positions of the particle were simulated: At the center of the hole, and off-centered in the $x$-direction and $y$-direction, touching the hole wall. The radius of the particle was set to 60 nm, similar in size to defect A. It is set to have a refractive index of 2, corresponding to $Si_3N_4$. Simulations with three different particle radii, centered both laterally and vertically in the center hole, were also done. Nominally, the radius of the particles were 40, 60 and 80 nm. Due to the discrete spatial resolution in the FDTD simulations, the actual simulated volumes of the particles were $2.4 \cdot 10^5$, $8.8 \cdot 10^5$, and $20.6 \cdot 10^5$ nm$^3$. We will refer to these particle sizes as $V_S$, $V_M$, $V_L$, in the following text.

The procedure of simulating a crystal of finite size is computationally intensive. Using periodic boundary conditions and a smaller simulation domain would speed up the simulations, and should be chosen if the aim is to investigate the effect of inserting a particle in every hole in a pristine PC, or every other, third, etc. In contrast to such investigations, we aim to find the effect of inserting one single particle in a pristine PC, for the case when a small fraction of the scattered light is emitted from the hole with the particle, and many holes around the particle emit scattered light. Even when terminating our $15 \times 15$ periods domain with periodic boundary conditions, and simulating the effect of inserting one particle in the center of this super cell, it is hard to extract the separate contribution from each particle. In order to see their contributions independently, we have therefore chosen to terminate the boundaries with PML, and hence been able to visualize the outward flow of optical power along the membrane from the particle.
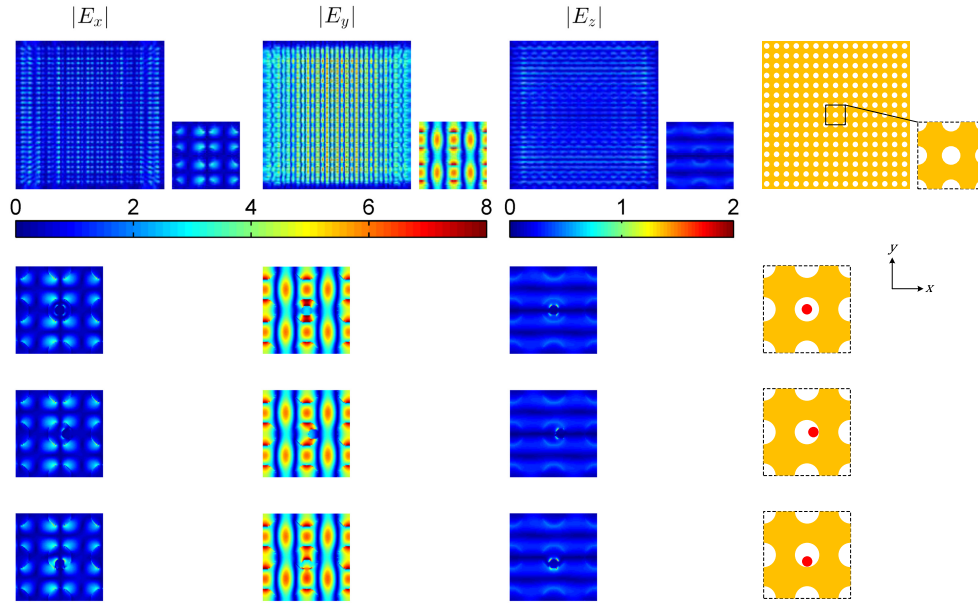
Fig. 4. Color image representations of fields resulting from continuous wave FDTD simulations of a pristine photonic crystal, illuminated with normal incidence $y$-polarized light at a wavelength of 703.6 nm, without a particle in the lattice (row 1), and photonic crystals with a particle inserted at three selected lateral positions in the center hole: Center (row 2), off-centered in the $x$-direction (row 3), and off-centered in the $y$-direction (row 4). The first three columns show the absolute value of the field components $E_x$, $E_y$, and $E_z$, respectively. Illustrations in the fourth column, corresponds to the areas in-plane over which the field has been plotted. The color scales represent the amplitude (absolute value) of each of the three components of the E-vector, divided by the amplitude of the E-vector of the incident plane wave.

### 3.1. Position dependence of particles trapped in photonic crystals

The FDTD simulations for a single wavelength (contiuous wave) allow us to compute an electric field vector, **E**, as a function of position. The vector **E**, has three components $E_x$, $E_y$, and $E_z$, each component being a complex phasor representing the amplitude and the phase relative to the incident wave. The upper row of field plots in Fig. 4, shows $|E_x|$, $|E_y|$, and $|E_z|$ in the center plane of a pristine PC. The excited guided resonance mode forms as rows of holes parallel to the incident polarization oscillate in phase and couple to a mode with in-plane $k$-vectors parallel to the $x$-axis. Since the boundaries of the simulation are terminated with absorbing walls, we are not simulating an infinite lattice, which is why the mode field declines as we approach the edge of the crystal [29]. The lower three rows in Fig. 4, show what happens when a particle is inserted in the crystal: The mode field is retained, and the effect of the particle is only visible in the immediate vicinity of the particle.

To clarify the change in fields, the absolute value of the change, $|\Delta \mathbf{E}| = |\mathbf{E}(\text{PC with particle}) - \mathbf{E}(\text{pristine PC})|$, is plotted in Fig. 5, for all three field components and particle positions. The plots show that the particle behaves similar to an ideal dipole: Inside the holes, the dominant field component of the mode field lies in-plane, pointing in the $y$-direction. The particle radiates spherical waves in the shape of a torus, with its axis of symmetry oriented parallel to the $y$-axis. It hence radiates strongly in the $x$-direction, and very weakly in the $y$-direction. The scattered light can either exit directly out into the surrounding
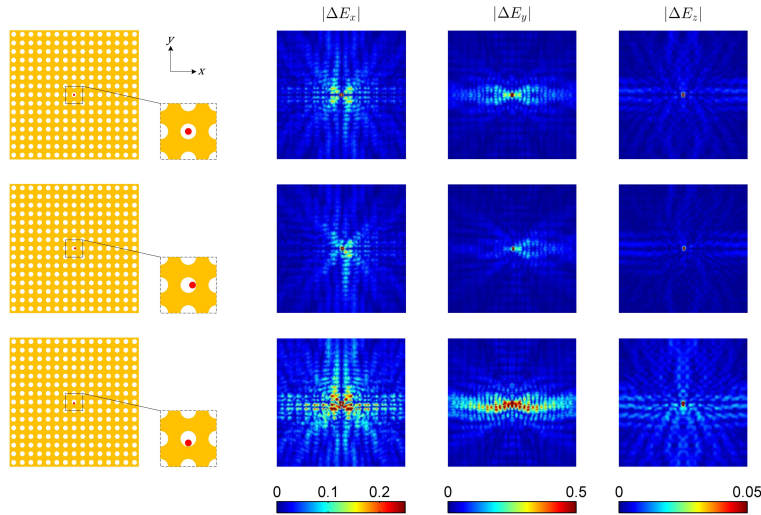
$|\Delta E_x|$  $|\Delta E_y|$  $|\Delta E_z|$

0  0.1  0.2    0    0.5    0    0.05

Fig. 5. Color image representations of absolute values of changes in the complex-valued field components $E_x$, $E_y$ and $E_z$, at the center plane of a pristine photonic crystal, caused by inserting a particle in the crystal. The photonic crystal is illuminated with normally incident $y$-polarized light at a wavelength of 703.6 nm. Three selected lateral positions of the particle in the center hole have been investigated: Center (row 1), off-centered in the $x$-direction (row 2), and off-centered in the $y$-direction (row 3). Illustrations to the far left correspond to the areas in-plane over which the field has been plotted. The change has been calculated by subtracting the field distribution for a pristine photonic crystal shown in Fig. 4 (top row), from the field distribution in a photonic crystal with a particle trapped in the lattice, Fig. 4 (row 2-4). The plotted fields hence correspond directly to the E-field scattered by the particles. The color scales represent the absolute value of the change in of each of the three components of the E-vector, divided by the amplitude of the E-vector of the incident plane wave.

medium, or couple to guided resonance in the membrane. The torus shape of the radiation diagram of an oscillating dipole in free space, will therefore be strongly distorted, but we still expect to see high $|\Delta E|$-values perpendicular to the axis of polarization, and very low $|\Delta E|$-values parallel to the axis of polarization. This symmetry is clearly present in Fig. 5, especially in the $|\Delta E_y|$-plot.

Moreover, there is an increase in $|\Delta E|$ as the particle is moved towards the wall in the $y$-direction where the guided-resonance mode field is maximized, and a decrease as the particle is moved towards the wall in the $x$-direction where the mode field is minimized. Finally, note that scattered light from a particle close to a wall, shows stronger coupling to the side where the wall is closest to the particle.

### 3.2. Size dependence of particles trapped in photonic crystals

Going from left to right in Fig. 6(a), plots show the absolute value of the change in the $y$ component of the vector **E**, $|\Delta E_y| = |E_y(\text{PC with particle}) - E_y(\text{pristine PC})|$, caused by inserting particles with volumes $V_S$, $V_M$, and $V_L$ in the center hole of a pristine PC. Qualitatively, all particle sizes induce the same change in field distribution. This is also the case for the $x$ and $z$ component of the field (not shown). The volume dependence is clarified in Fig. 6(b), showing a line plot of normalized field strengths from Fig. 6(a) superimposed on each other along the $x$-direction at $y = 0$.
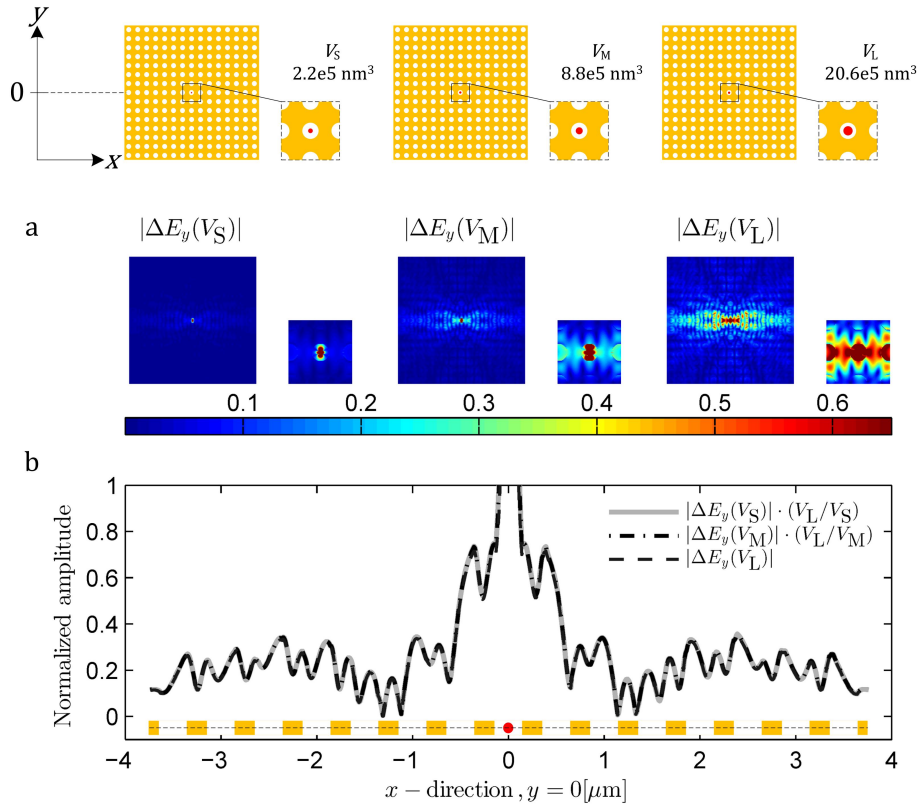
Fig. 6. (a) Color image representation of the $y$ component of the field at the center plane of a pristine photonic crystal illuminated with normal incidence $y$-polarized light at a wavelength of 703.6 nm, caused by inserting a particle in the center hole of the crystal. Three different particle sizes have been simulated, as shown in the three illustrations at the top. (b) Line plot crossing the field plots in (a) in the $x$-direction at $y = 0$. The color scale in (a) and the abscissa in (b) both represent the absolute value of the change in $E_y$ divided by the amplitude of the incident plane waves.

The field change resulting from the largest particle is scaled with 1, the medium particle with $V_L/V_M$ and the smallest particle with $V_L/V_S$. In the holes where the particle is located, the near field dominates the field distribution, and the plots do not overlap. A period away from the center hole the line plots are virtually overlapping, meaning the amplitude of the change is proportional to the particle volume.

We point out that forbidden asymmetries are visible especially in the plots showing $|E_x|$ for the pristine PC in Fig. 4 and $|\Delta E_x|$ for the centered particle in Fig. 5. It has been verified, by increasing the grid resolution for selected structures, that these asymmetries are dominantly caused by numerical errors attributed to insufficient grid resolution. We also note that PML does not work well for waves having $k$-vectors parallel to the PML [28]. The presence of such waves in the simulations is known to give rise to unphysical reflections from the boundary. The effect is present in our simulations, but is too weak to be visible in Figs. 4–6.

## 4. Experiment

Employing the two linear polarizers, $L_s$ and $L_d$, included in the optical setup illustrated in Fig. 1(d), enables polarized excitation, and cross-polarized excitation and detection. The source is in this case a diode laser producing a 1.1 mrad divergence collimated beam with a line width of $\sim$4.5 nm centered at 632 nm. The center wavelength corresponds to that of the desired guided resonance mode.

In the following results, microscope images have been recorded using two different polarizer configuration: Polarized excitation and unpolarized detection, where only polarizer $L_s$ is applied, and cross-polarized excitation and detection, where both polarizers, $L_s$ and $L_d$, are applied, and the source polarization is perpendicular to the detected polarization.

Eight recordings of the PC displayed in Fig. 2, are given in Figs. 7(a) and 7(b). One image displays the entire matrix of holes, and a smaller cut, labeled D, frames the immediate vicinity of defect A. Images in Fig. 7(a) are recorded using only polarizer $L_s$, and images in Fig. 7(b) are recorded with cross-polarized excitation and detection. Each row holds results for a fixed orientation of polarizer $L_s$, and arrows drawn on-top of a 3×3 hole matrix show the orientation of $L_s$ and $L_d$ relative to the lattice. The color scale shows the transmission, found by recording an image of the PC and dividing each pixel value by the mean background pixel value, found by recording an image without the PC in the light path.

A measure of the signal-to-background ratio (SBR) in each recoding is also displayed in Fig. 7. It has been calculated in the following way: Two sets of pixels with the same size were defined, corresponding to the area holding defect A [pixels D] and an area with hardly any observable defects [pixels M]. The locations of pixels D and M are the same in all recordings and have been marked with white frames labeled M and D, at the top left image in Fig. 7. The mean-, $M_{mean}$, and rms-value, $M_{rms}$, of pixels M, and the maximum value in pixels D, $D_{max}$, is found, and the signal-to-background ratio defined as SBR $= (D_{max} - M_{mean})/M_{rms}$.

The difference between the two polarizer configurations is clarified in Fig. 7(c), which holds line plots for both unpolarized detection and cross-polarized excitation and detection. The lines cross the recorded images in the $y$-direction, intersecting the peak in intensity in pixels D. The $x$-axis represents optical power per pixel, obtained by dividing each bit-value in the picture file by the exposure time.

### 4.1. Polarization dependent scattering from particles trapped in photonic crystals

The appearance of defect A for polarized excitation and unpolarized detection is shown in Fig. 7(a). As for unpolarized excitation and detection, resulting in the image in Fig. 1(c), the defect produces an ensemble of bright spots that coincide with the lattice. Light scattered by defect A is observed as a maximum, corresponding to the location of the defect, and scattered light coupled into the membrane, guided away from the defect center, is observed as re-scattering from the surrounding holes. However, in contrast to the pattern in Fig. 1(c), the symmetry of the patterns in Fig. 7(a) is not four fold symmetric. As predicted by the simulation results in Figs. 5 and 6, it is only two fold symmetric. Weaker scattering is observed from holes neighboring the defect along the line parallel to the incident polarization.

### 4.2. Decreasing background signal using cross-polarized excitation and detection

The signal-to-background ratio, is calculated to be 60, 80, 64 and 47 for the four different incident polarizations with unpolarized detection. Looking at the images in Fig. 7(a), the background signal is mainly limited by the non-zero and inhomogeneous transmittance of the membrane.

Using crossed polarizers, the signal-to-background ratio is changed to 91, 57, 147 and 97, respectively. The background signal is hence on average decreased relative to detected particle
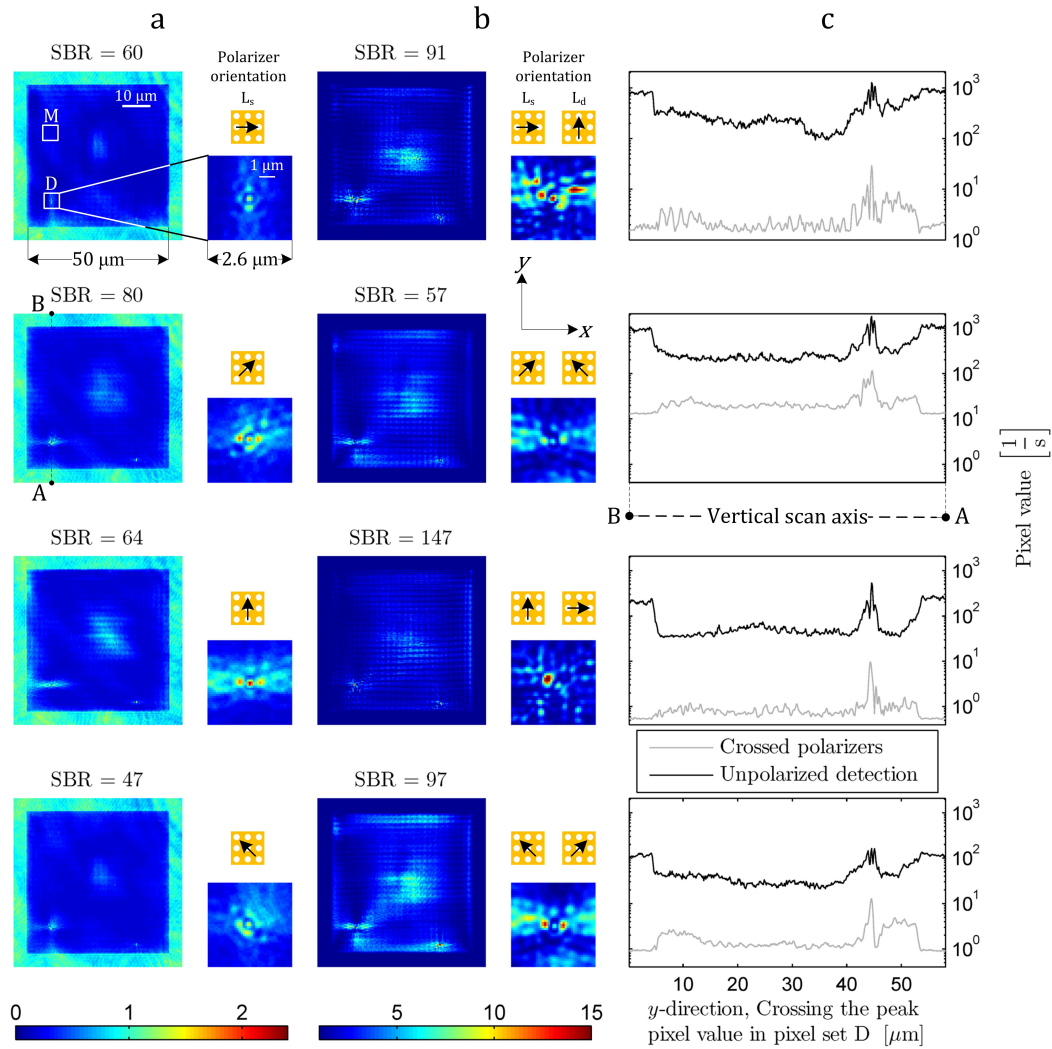
Fig. 7. Images recorded with the optical setup illustrated in Fig. 1(d). (a and b) Results are collected for four orientations of polarizer $L_s$, with polarizer $L_d$ (a) not employed and (b) oriented orthogonal to $L_s$. Arrows drawn on-top of a $3 \times 3$ hole matrix show the orientation of $L_s$ and $L_d$ relative to the lattice, for each recording. A set of pixels D, corresponding to the position of defect A has been enlarged, for every recording. The color scales located at the bottom of column (a) and (b) show the transmittance of the membrane, calculated by dividing the pixel values resulting from a recording of the membrane, by the mean pixel value in a recording without the membrane in the light path. (c) Line plots of pixel values, going from point A to B, crossing the crystal in the $y$-direction, intersecting the peak in pixel value in pixels D. The ordinate in the plots in (c) represents optical power per pixel, computed by dividing each bit-value in the picture file by the exposure time.

irradiance, and mainly created by two sources of unwanted depolarization: Depolarization at the lattice boundaries and at numerous localizable points across the membrane.

## 5. Discussion

We have so far only focused on defect A. The two other defects or contaminations seen in the lower and upper part of of Fig. 1(a), are not reported on in this study. This is because these defects cannot be considered to resemble molecular capture events. They are both too large with respect to Rayleigh small particle scattering theory, and also lie close to the lattice boundary, where the PC performance suffers from edge effects. We also note that in biosensing it is most relevant to focus on detection of nano-particles in water. However, in this proof of principle study, we have chosen to design the PC for detecting nano-particles in air. A discussion on what needs to be done in order for the sensor to be used to detect nano-particles in water is found in previous work [17].

In our particular design, incident light couples to a guided resonance mode that supports high fields in the holes. Simulation results in Fig. 2(c), show how the mode field in the holes can be considered as a driving field that has a dominant component parallel to the incident polarization. Figures 4 and 5 show how this driving field causes particles that are trapped in the holes to scatter, but is only locally affected by the presence of the particle. In Fig. 6(c), it is evident that the field in the hole where the particle is located, is strongly perturbed due to the near-field of the scattering particle, but in the closest neighboring holes to the particle, the mode field is approximately retained. Even for the largest particle, causing the largest change in the field, the maximum amplitude of the $y$ component of the scattered irradiation is 0.7 times the amplitude of the incident field. This is only 0.2 times the absolute value of the $y$ component of the resonantly enhanced E-field at the center plane of the membrane, averaged over one unit cell.

The reason for the spot pattern coinciding with the lattice can be explained by two distinguishable effects. One, light scattered from defect A cannot only radiate out into the medium surrounding the membrane. Part of the scattered irradiance can couple to the membrane and be guided away from the hole where defect A is located. This light will re-scatter when it meets neighboring holes. For unpolarized normal incidence light, as is used to obtain the image in Fig. 1(c), spherical waves will hence radiate out into the surrounding media directly from defect A, and from the nearest neighboring holes. The center spot in the pattern is directly related to scattered irradiance from defect A, and has an observed intensity set by the mode field amplitude at its location. Surrounding spots are a result of scattering from holes neighboring defect A, driven by the irradiance from defect A coupling to the membrane. Two, the light that is coupled out of the membrane via scattering by defect A, is dominantly drawn from the guided resonance mode. Consequently, the mode phase-matched to interfere destructively with directly transmitted light looses some of its power. This power is also locally bound to defect A and can create a spot pattern that coincides with the symmetry of the lattice.

### 5.1. *Dipole like behavior of particles trapped in photonic crystals*

We have previously proposed that the spatial distribution of the scattered light is similar to an ideal dipole, with the zero-field axis aligned with the driving field. Field plots in Figs. 5 and 6 support that this is the case. Particles trapped in the lattice scatter dominantly perpendicularly to the polarization of the driving field. These simulation results also agree with the experimental observation in Fig. 7(a), showing the result of polarized excitation. Strong scattering is seen from the hole where the defect is located, and from the neighboring holes, going out from the defect center, in a direction perpendicular to the incident polarization. Weaker scattering is seen from the holes, going out from the defect center, in a direction parallel to the incident polarization. Consequently, all images displayed in Fig. 7(a) show spot patterns with two folded symmetry. The minor deviations from two folded symmetry, can be explained by the off-centered position of defect A in the hole. This also agrees with the simulation results

in Fig. 5, where it is evident that scattered light from the defect couples stronger to the side where it is touching the hole wall. Hence, we see stronger scattering from the lower and left neighboring holes.

Since we only have one PC holding one ideal test particle, we have not been able to verify experimentally the size dependence evident in Fig. 6. Furthermore, our simulation results show that the direction of propagation and strength of scattered light from the defect is strongly dependent on its position in the hole, and we have not been able to find a non-destructive method to determine the chemical composition of our defect. We therefore hesitate to infer anything about permittivity and size of our defect from our measurements.

The $|\Delta E|$-plots in Fig. 6(b) show that the amplitude of the scattered light is proportional to the volume of the scattering particle, and results presented in Fig. 5 show how the scattered amplitude is increased when the particle is moved into areas with a stronger driving field. This complies with Rayleigh scattering theory [30], which says that the amplitude of scattering from isolated particles is proportional to the volume of the scattering particle and the amplitude of the driving field. Since the intensity recorded by the CCD camera in our optical setup is the field amplitude squared, the sensitivity of the sensors is proportional to the volume of particles squared, and can be improved by increasing the amplitude of the driving field.

## 5.2. *Decreased background signal by use of crossed polarizers*

As shown by the zero-transmission dip at 631 nm in Fig. 2(b), an infinite pristine PC can function as a mirror. When a particle is present in the lattice, it can therefore be observed in transmission as a bright spot, or a group of spots, on a background that in theory can be made black. In practice, the reflectivity is limited by fabrication accuracy, finite extent of the lattice, non-zero divergence of the excitation source and a finite source bandwidth. The minimum transmittance in our experiments is consequently closer to 20%, as can be seen in Fig. 7(a). This relatively high background, in combination with a sensitivity that is proportional to the volume of the particles squared, is limiting. As particles are reduced in size, the scattered light they produce falls fast below the noise floor. Alternative methods for reducing the background signal are therefore needed.

Experimental results presented in Fig. 7 show how cross-polarized excitation and detection is an alternative, that increases the signal-to-background ratio by up to a factor of three. This method is especially well suited in our design. For normal incidence plane waves, incident on a square 2D PC, the symmetry of the lattice forces the reflected and transmitted fields to retain the original polarization in the far-field. If the orthogonal polarization is present in transmission, it must originate from defects in the crystal or from imperfect extinction present in the measurement setup independent of the membrane. Cross-polarized excitation and detection hence filters out all but exactly what we are looking for, namely defects in the crystal.

It is further possible to argue that our signal-to-background ratio is a modest estimate. The calculated rms-value of the background, does not only include noise related to the detector chip. Although it is found by sampling an area with little defects, there is a contribution from lattice discrepancies. The sensor is meant to capture biomolecules. Detection is done by comparing the transmittance of the membrane before and after a molecule is captured, subtracting the initial image from the image taken after capture. By this procedure, contributions to the background signal from static defects in the crystal can be removed and lead to an increased signal-to-background ratio.

As seen in Fig. 7(b), displaying results from measurements using cross-polarized excitation and detection, depolarization of the incident light is observed at numerous localizable points across the membrane. The points lie along lines parallel to the PC lattice axes, and we believe they are a result of deviations in lattice period, hole radius and hole shape. These structural

discrepancies cannot be seen using SEM. The assumption hence implies that the current background signal is mainly limited by fabrication accuracy of the PC, and the sensitivity of the sensor exceeds the resolution of our SEM, i.e. we should be able to detect 20-40 nm diameter particles. This also agrees with the calculated signal-to-background ratio, which predicts that the detection limit is close to 26.1 nm: $r_{\min} = \left(r_p^6/\mathrm{SBR}_{\max}\right)^{1/6} = \left((60\pm15 \text{ nm})^6/147\right)^{1/6} = 26.1\pm6.5$ nm.

This detection limit allows us to detect particles the size of single viruses. The sensitivity of the sensor hence has to be improved in order to detect proteins, which typically have a radius of 2-10 nm. This presents a challenge, since the sensitivity is proportional to the volume of trapped particles square. The sensitivity can however be improved by increasing the amplitude of the driving field, which can be done by utilizing a guided resonance mode with a higher Q-factor. An increased Q-factor of guided resonance modes can be achieved by decreasing the scattering strength of the PC. In practice, it is a question of production accuracy, and can e.g. be done by reducing the size of the holes in the PC [19, 31].

## 6. Conclusion

We have designed, fabricated, and characterized a PC that can be used as a nano-particle sensor. The key component in our scheme is a photonic crystal membrane supporting guided resonance modes. Simulation and experimental results presented in this report, show how detection is a result of amplified small particle scattering. Small particles trapped in photonic crystals, excited by normal incident light coupling to a guided resonance mode, scatter similar to ideal dipoles.

Provided a chemistry that facilitates capturing of biomolecules, the current design should enable detection of single viruses. The design is simple and composed of standard optical components, allowing it to be made cheap. It can also be made compact, by replacing the microscope by a set of lenses specific to the application. Further optimization of the design is needed to reach the sensitivity level of targets like proteins.

## Acknowledgments